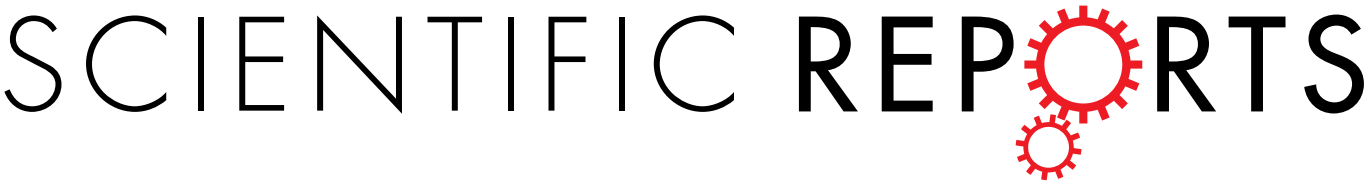

OPEN

Modulated $CH_3NH_3PbI_{3-x}Br_x$ film for efficient perovskite solar cells exceeding 18%

Received: 22 December 2016
Accepted: 09 February 2017
Published: 17 March 2017

Yongguang Tu, Jihuai Wu, Zhang Lan, Xin He, Jia Dong, Jinbiao Jia, Panfeng Guo, Jianming Lin, Miaoliang Huang & Yunfang Huang

The organic-inorganic lead halide perovskite layer is a crucial factor for the high performance perovskite solar cell (PSC). We introduce CH_3NH_3Br in the precursor solution to prepare $CH_3NH_3PbI_{3-x}Br_x$ hybrid perovskite, and an uniform perovskite layer with improved crystallinity and apparent grain contour is obtained, resulting in the significant improvement of photovoltaic performance of PSCs. The effects of CH_3NH_3Br on the perovskite morphology, crystallinity, absorption property, charge carrier dynamics and device characteristics are discussed, and the improvement of open circuit voltage of the device depended on Br doping is confirmed. Based on above, the device based on $CH_3NH_3PbI_{2.86}Br_{0.14}$ exhibits a champion power conversion efficiency (PCE) of 18.02%. This study represents an efficient method for high-performance perovskite solar cell by modulating $CH_3NH_3PbI_{3-x}Br_x$ film.

Recent years, the solar cells based on organic-inorganic lead halide perovskite are considered as one of the most important developments in the field of solar energy due to their many advantages including low cost, facile preparation process, good stability and high power conversion efficiency (PCE)[1–4], meanwhile, organic-inorganic lead halide perovskite unique feature such as broad and strong light absorption[5], longer carrier lifetimes[6], long charge carrier diffusion length[7,8], and low exciton binding energy[9]. The perovskite solar cells (PSCs) are generally composed of transparent conducting oxide substrate (TCO), a n-type compact blocking layer, alkylammonium lead halide perovskite layer with or without scaffold layer, a p-type hole-transporting material (HTM) layer and a metal back electrode[1,2]. To date, the power conversion efficiency (PCE) of PSC has reached 20.8%[10]. More recently, the highest reported PCE of PSCs has reached 22.1%[11].

The perovskite layer is a crucial factor for the high performance perovskite solar cells[1,2,12,13] because perovskite as light harvester absorbs incident irradiation, its energy level dominates the photovoltage and photocurrent of the device, and its morphology affects the charge carrier transportation and the photoelectric properties of the solar cells. Perovskite layers mainly are prepared by sequential deposition[14], solvent engineering[15], vapour-assisted deposition[16], and vacuum evaporation[17]. The most-studied perovskite layers are $CH_3NH_3PbI_3$[18], $CH_3NH_3PbI_{3-x}Cl_x$[19], $CH_3NH_3PbBr_3$[13], etc. Noticeably, most high efficiency perovskite solar cells are based on $CH_3NH_3PbI_3$ or $CH_3NH_3PbI_{3-x}Cl_x$ perovskites[20]. Engineering halide perovskite through mixing halogen elements, such as $CH_3NH_3PbI_{3-x}Cl_x$ and $CH_3NH_3PbI_{3-x}Br_x$, is a viable way to increase the perovskite stability, enhance carrier transport and turn band gap[21]. Recently, $CH_3NH_3PbI_{3-x}Br_x$ based on perovskite solar cells have drawn much attention owing to their variable energy band gaps by adjusting the bromide-iodide ratio[22]. However, the power conversion efficiencies of the perovskite solar cells based on $CH_3NH_3PbI_{3-x}Br_x$ are still lower[21]. As examples, Seok *et al.* reported the meso-structured perovskite solar cells with a PCE of 12.3% by utilizing the traditional one-step spin-coating method for $CH_3NH_3PbI_{3-x}Br_x$ deposition[22]. Huang *et al.* achieved a PCE of 13.1% in $CH_3NH_3PbI_{3-x}Br_x$-based planar perovskite solar cells by using the two-step spin-coating method with the solvent annealing process[23]. Yuan *et al.* achieved a high fill factor exceeding 85% and a power conversion efficiency exceeding 13% in $CH_3NH_3PbI_{3-x}Br_x$ based perovskite solar cells[20].

Herein, we introduce CH_3NH_3Br in the precursor solution to prepare mixed methylammonium lead halide $CH_3NH_3PbI_{3-x}Br_x$, which results in the significant improvement of photovoltaic performance of PSCs. Firstly, uniform perovskite layer with improved crystallinity and apparent grain contour is obtained, less grain boundaries will facilitate the transmission of charge. Secondly, owing to the introduction of Br into $CH_3NH_3PbI_3$, the

Engineering Research Center of Environment-Friendly Functional Materials for Ministry of Education, Institute of Materials Physical Chemistry, College of Material Science and Engineering, Huaqiao University, Xiamen 361021, China. Correspondence and requests for materials should be addressed to J.W. (email: s: jhwu@hqu.edu.cn)

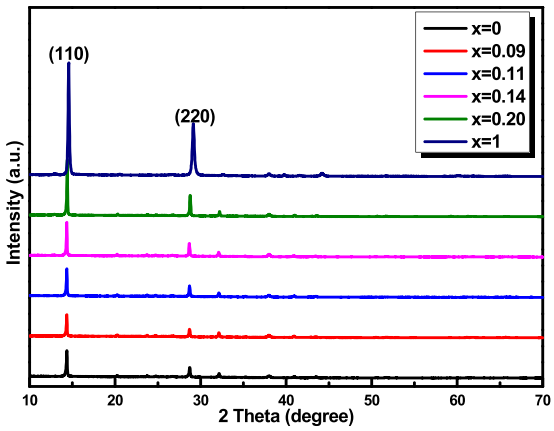

Figure 1. XRD patterns of $CH_3NH_3PbI_{3-x}Br_x$ perovskite films.

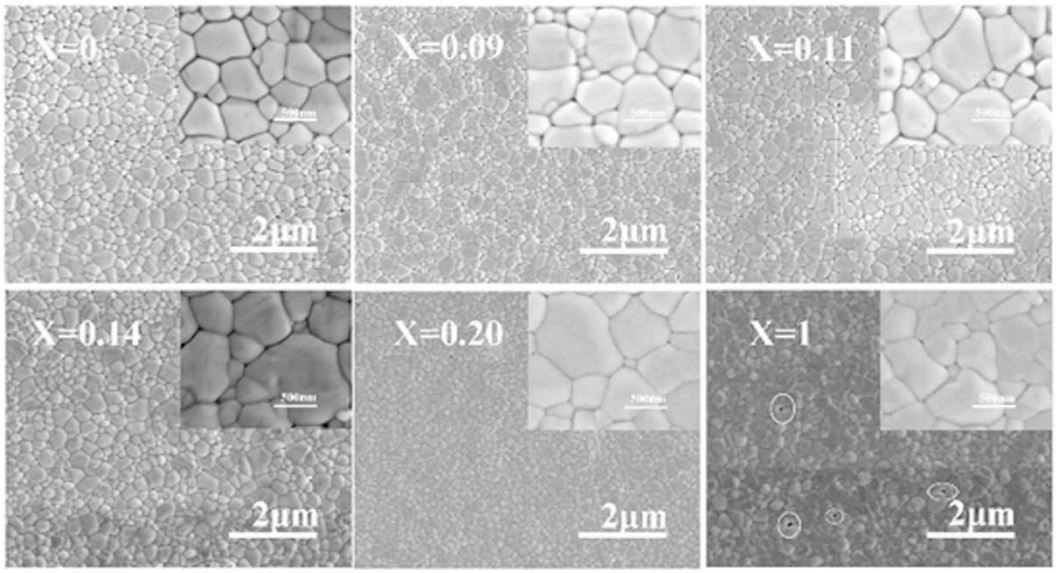

Figure 2. Top-view SEM images of $CH_3NH_3PbI_{3-x}Br_x$ perovskite films.

energy band of perovskite is expanded and leads to a higher photovoltage (V_{OC}) of the device. Thirdly, the modulation of Br is beneficial to the interfacial energy match between TiO_2/perovskite/spiro-OMeTAD, the injection and extraction of charge carriers are improved and thus the photocurrent and fill factor of the device are enhanced. Under optimal conditions, the device with $CH_3NH_3PbI_{2.86}Br_{0.14}$ exhibits high reproducibility and a champion PCE of 18.02%.

Results

Crystallinity and morphology. $CH_3NH_3PbI_{3-x}Br_x$ perovskites were prepared by controlling different iodide/bromide molar ratio in perovskite precursor solutions. The resultant mixed methylammonium lead halides are termed as $CH_3NH_3PbI_3$, $CH_3NH_3PbI_{2.91}Br_{0.09}$, $CH_3NH_3PbI_{2.89}Br_{0.11}$, $CH_3NH_3PbI_{2.86}Br_{0.14}$, $CH_3NH_3PbI_{2.8}Br_{0.2}$, and $CH_3NH_3PbI_2Br$, respectively. Figure 1 shows the XRD patterns of the $CH_3NH_3PbI_{3-x}Br_x$ perovskite films. The two main peaks for all $CH_3NH_3PbI_{3-x}Br_x$ films approximately located at 14.2° and 28.4° can be indexed to the (110) and (220) planes[24,25], confirming the presence of the tetragonal perovskite phase in all of the prepared films. In order to examine the influence of Br amount on the crystallinity of the perovskite films, XRD patterns of $CH_3NH_3PbI_{3-x}Br_x$ films at 13.5°~15.5° were measured and shown in Figure S1. The FWHM values of the strong diffraction peaks of the (110) face are calculated using JADE 6.0[26,27]. The FWHM values of the $CH_3NH_3PbI_{3-x}Br_x$ films are 0.17°, 0.18°, 0.16°, 0.14°, 0.13° and 0.12°, corresponding to the $CH_3NH_3PbI_{3-x}Br_x$, x = 0, 0.09, 0.11, 0.14, 0.20, and 1, respectively. Small FWHM value means a sharper XRD pattern[28–29]. On the other hand, the characteristic (110) peak has shifted from $CH_3NH_3PbI_3$ at 14.30° to $CH_3NH_3PbI_2Br$ at 14.09°, corresponding to a reduction in the lattice parameter from a = 0.616 nm to a = 0.604 nm with the increase in the Br content due to the difference in the ionic radius of Br^- (1.96 A) and I^- (2.2 A), which is consistent with the literatures[22,30].

Top-view SEM images of as-prepared $CH_3NH_3PbI_{3-x}Br_x$ hybrid perovskite films are shown in Fig. 2. It can be seen that the Br amount has a mild influence on the grain size of the hybrid perovskite. $CH_3NH_3PbI_{2.86}Br_{0.14}$ and

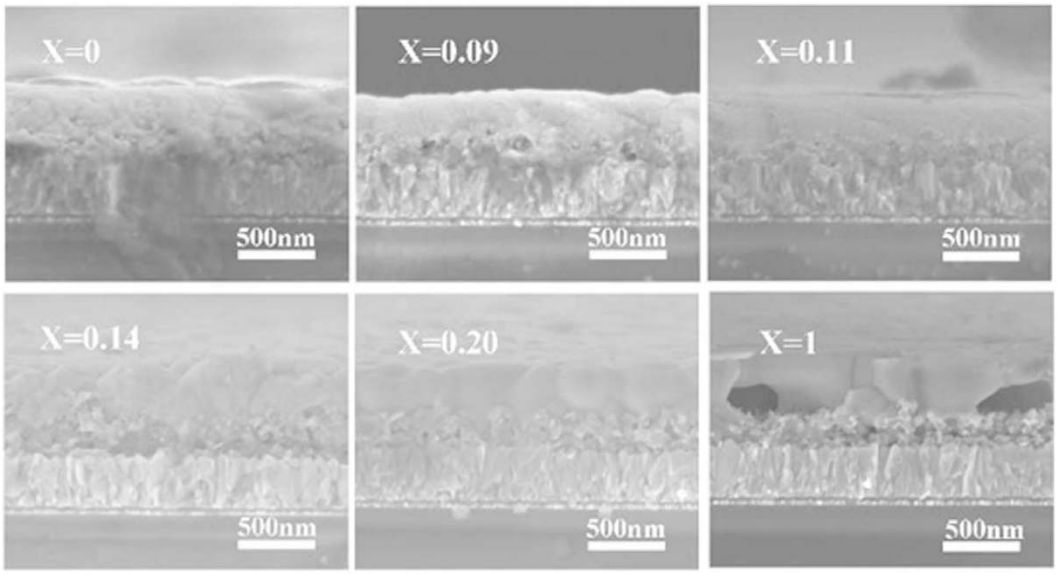

Figure 3. Cross-view SEM images of $CH_3NH_3PbI_{3-x}Br_x$ perovskite films.

$CH_3NH_3PbI_{2.8}Br_{0.2}$ present compact, pinhole-free perovskite films and enlarged average grain size, which will minimize the grain boundary energy and be beneficial to the charge transportation. For $CH_3NH_3PbI_2Br$, there are some pinholes appearing in the film, marked by white circles. The pinholes will produce direct contacts of spiro-OMeTAD and electron transporting layer, leading to a shunting path which probably decreases fill factor and open-circuit voltage for the device with $CH_3NH_3PbI_2Br$[17].

Figure 3 shows the cross-view SEM images as-prepared $CH_3NH_3PbI_{3-x}Br_x$ perovskite films. Surprisingly, there are some stark contrasts of the perovskite film in vertical direction. The cementite appears as small granular grain in the capping perovskite layer for $CH_3NH_3PbI_3$ and $CH_3NH_3PbI_{2.91}Br_{0.09}$. With the increase of Br amount from $CH_3NH_3PbI_3$ to $CH_3NH_3PbI_2Br$, the big grain contour becomes gradually obvious. The grain size is commensurate with its thickness among $CH_3NH_3PbI_{2.86}Br_{0.14}$, $CH_3NH_3PbI_{2.8}Br_{0.2}$ and $CH_3NH_3PbI_2Br$, most of the grain boundaries are perpendicular to the mesoporous layer to minimize the grain boundaries. As well known that the less grain boundaries will facilitate the transportation of charge[29,31], thus it is expected that the fill factor of the corresponding device is improved by adjusting Br amount in $CH_3NH_3PbI_{3-x}Br_x$ hybrid perovskite.

However, for $CH_3NH_3PbI_2Br$, there are many voids at the bottom of the perovskite layer which may be attributed to the dewetting during anti-solvent washing and subsequent growth[29,31,32]. In the specific experimental operation of $CH_3NH_3PbI_2Br$, the viscosity of the precursor solution may vary owing to different compositions in the precursor solution and the methylammonium halide was composed entirely of MABr. As the nucleation grows the material dewets at the interface between solution-phase and solid-phase, meaning that it is pulled away from the regions surrounding the crystals, resulting in the formation of large voids in the film. So a distinguishing crystallization behavior was obtained without MAI in the precursor solution. Many voids in the perovskite layer will result in inferior photovoltaic performance of PSCs.

Band gap. Figure 4 shows the UV-visible absorption spectra of the $CH_3NH_3PbI_{3-x}Br_x$ perovskite films with different iodide/bromide ratio. It can be seen that with the increase of Br amount from $CH_3NH_3PbI_3$ to $CH_3NH_3PbI_2Br$, the absorption edges of the hybrid perovskite films shift towards the shorter wavelength[33]. The bandgaps of crystallized perovskite films are 1.565, 1.579, 1.585, 1.591, 1.597, and 1.725 eV, corresponding to the $CH_3NH_3PbI_{3-x}Br_x$, $x = 0$, 0.09, 0.11, 0.14, 0.20, and 1, respectively, from the Taus plots[34] shown in Figure S2. The corresponding absorption edge and band gap are listed in Table 1. The blue shift is found that: 782 nm for $CH_3NH_3PbI_3$ is shifted to 709 nm for $CH_3NH_3PbI_2Br$, consistent with the variety of the energy band levels of perovskite materials in Figure S3. According to the literatures[34–36] and the energy level principle[2,3,12,37,38], with the increase of Br amount in $CH_3NH_3PbI_{3-x}Br_x$ the conduction band of the perovskite ascends and the valence band descends, resulting in the absorption edge shifted towards to shorter wavelength, which indicates the formation of wider energy band and a higher photovoltage (V_{OC}) of the device.

Charge carrier lifetime. Time resolved photoluminescence (TRPL) intensity decay measurements of $CH_3NH_3PbI_{3-x}Br_x$ perovskite films offer a quantitative information on the dynamics of charge carrier recombination[39], the samples were composed of FTO/CL-TiO_2/mp-TiO_2/perovskite, and corresponding results are presented in Fig. 5, of which the fitted time constants charge carrier lifetime (τ) are 52, 39, 35, 34, 33, and 15 ns, corresponding to the $CH_3NH_3PbI_{3-x}Br_x$, $x = 0$, 0.09, 0.11, 0.14, 0.20, and 1, respectively. The shorter τ value means that the charge more fast transfers from the perovskite to TiO_2 layer[40–44]. The significantly reduced τ value with the increase of Br amount in the hybrid perovskite infers an efficient charge extraction process occurred at the perovskite/TiO_2 interface. The $CH_3NH_3PbI_2Br$ yields the smallest τ value, meaning that the charge carriers extract very quickly, which may be attributed to the high conduction band of the perovskite. The high conduction

$CH_3NH_3PbI_{3-x}Br_x$	Absorption edge (nm)	Band gap (eV)	V_{OC} (V)	J_{SC} (mA·cm^{-2})	FF	PCE(%)
x = 0	782	1.565	1.016	22.92	0.67	15.60
x = 0.09	775	1.579	1.026	23.04	0.69	16.31
x = 0.11	772	1.585	1.052	23.08	0.69	16.75
x = 0.14	769	1.591	1.064	23.52	0.72	18.02
x = 0.20	766	1.597	1.065	22.95	0.70	17.11
x = 1	709	1.725	0.827	7.72	0.60	3.83

Table 1. Energy data and photovoltaic parameters of PSCs with $CH_3NH_3PbI_{3-x}Br_x$.

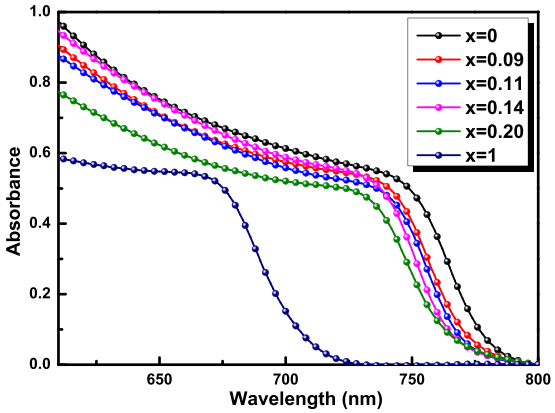

Figure 4. UV-visible absorption spectra of $CH_3NH_3PbI_{3-x}Br_x$ perovskite films.

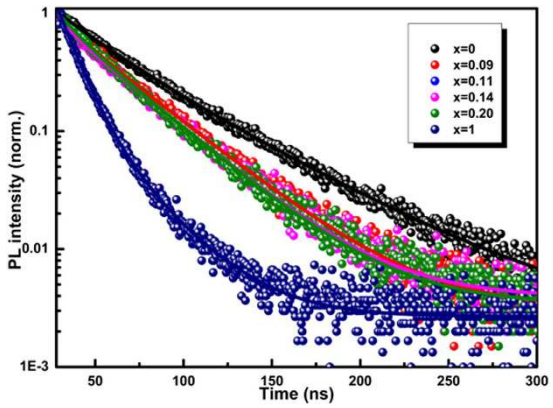

Figure 5. Time-resolved photoluminescence intensity decay of $CH_3NH_3PbI_{3-x}Br_x$ detected at peak emission wavelength of 760 nm.

band energy level is beneficial to the charge injection between the perovskite and the electron selective electrode, however, the device of $CH_3NH_3PbI_2Br$ presents the worst performance.

Charge transferring resistances. Nyquist plots of $CH_3NH_3PbI_{3-x}Br_x$ films are shown in Fig. 6, and the corresponding equivalent circuit is inset. The radius of semi-circles corresponds to the interfacial charge transfers resistance[45,46]. It can be seen that with the increase of X (Br amount), the radii first decrease, and then increase. When X = 0.14, the radius reaches the minimum, indicating the smallest interfacial charge transfers resistance among all $CH_3NH_3PbI_{3-x}Br_x$ films. Therefore, the device based on $CH_3NH_3PbI_{2.86}Br_{0.14}$ film possesses superior charge injection characteristics and low internal resistance, resulting in better photovoltaic performance than others.

Photovoltaic performance. *J-V* curves (reverse scan) of the perovskite solar cells based on $CH_3NH_3PbI_{3-x}Br_x$ hybrid perovskite are shown in Fig. 7 and the corresponding photovoltaic parameters are listed in Table 1. For the device based on ancestral $CH_3NH_3PbI_3$ film, a PCE of 15.60% is obtained with short-circuit current

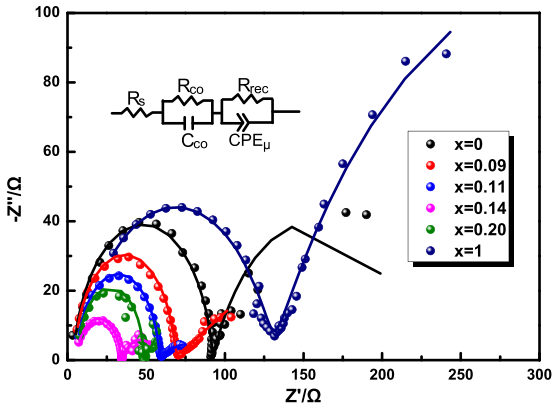

Figure 6. Nyquist plots of $CH_3NH_3PbI_{3-x}Br_x$ films.

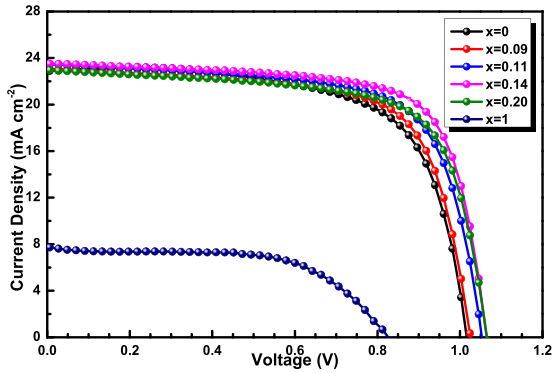

Figure 7. *J-V* curves of the PSCs based on $CH_3NH_3PbI_{3-x}Br_x$ under AM 1.5 G illumination.

density (J_{SC}) of 22.92 mA·cm^{-2}, open-circuit photovoltage (V_{OC}) of 1.016 V and fill factor (*FF*) of 0.67. For the devices based on $CH_3NH_3PbI_{3-x}Br_x$ films (x = 0~0.14), the performance continuously improve with the increase of Br amount. Best performance is achieved in the PSC based on $CH_3NH_3PbI_{2.86}Br_{0.14}$, yielding a J_{SC} of 23.52 mA·cm^{-2}, V_{OC} of 1.064 V, and *FF* of 0.72, resulting in a PCE of 18.02%. Further increasing the amount of Br in $CH_3NH_3PbI_{2.8}Br_{0.2}$ do not improve device performance, resulting from a lower J_{SC} of 22.95 mA·cm^{-2}. Furthermore, the performance of the device based on $CH_3NH_3PbI_2Br$ shows a dramatic downward.

The reason for the increase and then decrease of power conversion efficiency (PCE) of the PSCs with the increase of Br amount lies in V_{OC}, J_{SC} and *FF*. From the aspect of PV energy devices[3,17,37,38], with the increase of Br amount, the conduction band of the perovskite ascends and the valence band descends, the energy difference (ΔE_1) between TiO_2 Femi level and the valence band of perovskite expends, the energy difference (ΔE_2) between the conduction band of perovskite and TiO_2 Femi level also expends. The expanded ΔE_1 increases V_{OC}, however appropriate ΔE_2 produces small energy loss and large J_{SC} and FF; and excess ΔE_2 by excessive Br leads to an opposite result. From the aspect of morphology, owing to a large amount of voids in $CH_3NH_3PbI_2Br$ perovskite by dewetting, the charge extraction process is limited at the interface of perovskite/TiO_2. Combined above factors, photovoltaic parameters of the PSCs based on $CH_3NH_3PbI_{3-x}Br_x$ increase and then decrease of with the increase of Br amount.

Noticeably, owing to different preparation conditions, materials and devices structure, the optimized bromide/iodide ratio may be different. For example, Jeon *et al.* reported an optimal perovskite $CH_3NH_3PbI_{3-x}Br_x$ (x = 0.3~0.45)[15], and He *et al.* obtained an efficiency of 12.1% in planar heterojunction device by using $CH_3NH_3PbI_{2.4}Br_{0.6}$[47].

Figure S4 and Table S1 show the *J-V* curves and the photovoltaic parameters of the devices based on $CH_3NH_3PbI_{3-x}Br_x$ films (x = 0, 0.09, 0.14, and 1) under both reverse and forward bias scans. It can be seen that there are still noticeable hysteresis effects and instabilities for all samples. However, the device based on the champion film $CH_3NH_3PbI_{2.86}Br_{0.14}$ shows the highest reverse PCE (18.02%) and forward PCE (14.62%).

Statistic results of the cell performance are provided in Fig. 8 as histogram charts. It can be found that the devices with $CH_3NH_3PbI_{2.86}Br_{0.14}$ shows better performance and the average PCE is 17.37%. Meanwhile, the histogram chart demonstrates the high reproducibility of the devices (Each team is calculated from a batch of 50 cells). The corresponding incident-photon-to-current conversion efficiency (IPCE) spectra of PSC devices are shown in Figure S5.

J-V curves of the devices based on $CH_3NH_3PbI_{2.86}Br_{0.14}$ with various dwell time from 30 ms to 800 ms are shown in Figure S6, it can be seen that there are minor fluctuations. Figure S7 shows the steady-state photocurrent

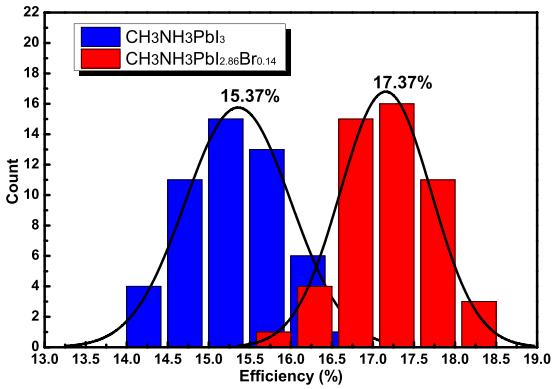

Figure 8. Histograms of the PCEs of the PSCs with $CH_3NH_3PbI_3$ and $CH_3NH_3PbI_{2.86}Br_{0.14}$.

and output PCE of the device based on $CH_3NH_3PbI_{2.86}Br_{0.14}$ at the maximum power points with a stabilized current density output of 20.10 mA·cm^{-2} (at the voltage of 0.88 V), yielding a PCE of 17.68%.

Discussions

In summary, we introduce CH_3NH_3Br in perovskite precursor solution to prepare $CH_3NH_3PbI_{3-x}Br_x$, leading to the significant improvement of photovoltaic performance of perovskite solar cell. Firstly, uniform perovskite layer with improved crystallinity and apparent grain contour is obtained, and less grain boundaries will facilitate the transportation of charges. Secondly, owing to the introduction of Br, the energy band of perovskite is expanded, resulting in a higher photovoltage of the device. Thirdly, the appropriate regulation of energy level by Br is beneficial to interfacial energy match and the charge injection and extraction at between TiO_2/perovskite/spiro-OMeTAD and enhances photocurrent, which is certified by time-resolved photoluminescence intensity decay measurements. Under optimal conditions, the device based on $CH_3NH_3PbI_{2.86}Br_{0.14}$ achieves a champion PCE of 18.02% with a stabilized output efficiency of 17.68% at the maximum power point.

Methods

Materials and Reagents. All of the materials were purchased from the Sigma-Aldrich Corp., if not specified. The Spiro-OMeTAD was from Luminescence Technology Corp. CH_3NH_3I was synthesized according to literature[48].

Precursor solution preparation. 461 mg PbI_2 (99.9985%, Alpha Aesar) and 78 mg DMSO were mixed in 702 μL DMF solution at room temperature. Then, mixed methylammonium halides (MAX, X = I, Br) were added to the above solution, the mole ratio of PbI_2: MAX: DMSO was controlled at 1:1:1. The molar ratio of MAI: MABr in MAX was controlled at: 1:0, 10:1, 8:1, 6:1, 4:1, 0:1, respectively. Lastly, the solutions were stirred at room temperature for 1 h in order to form a completely dissolved perovskite precursor solution. The resultant perovskites were termed as $CH_3NH_3PbI_3$, $CH_3NH_3PbI_{2.91}Br_{0.09}$, $CH_3NH_3PbI_{2.89}Br_{0.11}$, $CH_3NH_3PbI_{2.86}Br_{0.14}$, $CH_3NH_3PbI_{2.8}Br_{0.2}$, and $CH_3NH_3PbI_2Br$, respectively.

Device fabrication. Fluorine-doped tin oxide-coated (FTO) glass (Pilkington, TEC-8, 8Ω/sq) was cleaned by UV-ozone treatment for 15 min, followed by cleaning with detergent and ethanol consecutively. The compact TiO_2 blocking layers were deposited on FTO glass, which was prepared by spin-coating 0.15 M titanium diisopropoxide bis(acetylacetonate) (75 wt% in isopropanol, Aldrich) in 1-butanol (99.8%, Aldrich) solution, at 500 rpm for 5 s and 2000 rpm for 30 s and then dried at 125 °C for 5 min. A mesoporous TiO_2 film was deposited on compact TiO_2 layer by spin-coating TiO_2 paste diluted in ethanol. TiO_2 paste was prepared as described previously[49–51]. After drying at 100 °C for 5 min, the film was annealed at 450 °C for 30 min, providing a thickness of *ca.* 200 nm. The mesoporous TiO_2 film was immersed in 0.02 M aqueous $TiCl_4$ solution at 80 °C for 20 min. After washing with deionized water and alcohol, the film was heated at 500 °C for 30 min. 20 μL precursor solution was dipped onto the mesoporous TiO_2 layer and then spun at 4000 rpm for 25 sec. During spinning, 0.5 mL of diethyl ether was slowly dripped on the rotating substrate within the first 7 s. The film was finally heated to 60 °C for about 2 min and followed by 100 °C for 10 min.

A volume of 20 μL of 2,2′,7,7′-tetrakis (N,N-di-p-methoxyphenylamine) −9,9-spirobifluorene (Spiro-OMeTAD) solution was spin-coated on the $CH_3NH_3PbI_3$ perovskite layer at 4,000 rpm for 30 s. A Spiro-OMeTAD solution was prepared by dissolving 72.3 mg of Spiro-OMeTAD in 1 mL of chlorobenzene, to which 28.8 μL of 4-tert-butyl pyridine and 17.5 μL of lithium bis(trifluoromethanesulfonyl)imide (Li-TFSI) solution (520 mg LI-TSFI in 1 mL acetonitrile, Sigma-Aldrich, 99.8%) were added. All devices were stored in a desiccator (humidity < 15%) in the dark for 12 h. Finally, 80 nm of gold was deposited under vacuum through a shadow mask.

Characterization. The current density-voltage *(J-V)* curves were measured using a Keithley 2420 source-measure unit under AM1.5 G illumination at 100 mW·cm^{-2} provided by an Oriel Sol 3 A solar simulator in ambient environment. The light intensity was adjusted using a NREL-calibrated Si solar cell equipped with KG-2 filter. The devices had an active area of 0.125 cm^2 without metal mask. The devices were measured by reverse

(2.0 to −0.1 V) and forward (−0.1 to 2.0 V) voltage scanning at a scan step of about 21.2 mV (100 data points in total). The pre-sweep delay time was 40 ms, the dwell time at each voltage step was 30 ms. Surface morphologies were characterized by field-emission scanning electron microscopy (SEM, Hitachi S-8000, Japan). The crystalline structures were examined using X-ray diffraction (XRD, Bruker AXS, D8 Advance). Impedance spectra (IS) for the solar cell were measured on a ZAHNER IM6e electrochemical workstation under 1 sun AM 1.5 illumination, by applying a 0 V DC bias and a 5 mV voltage perturbation in the frequency range from 0.1 to 10^6 Hz. The impedance spectra were analyzed with Zview software. *IPCE* curves were measured as a function of wavelength from 300 nm to 800 nm using the Newport IPCE system (Newport, USA). The time-resolved photoluminescence spectrum was acquired using the time-correlated single-photon counting technique (Pico harp 300), and the excitation light pulse was provided using a picosecond diode laser at a wavelength of 760 nm with a repetition frequency of 1 MHz (PDL 800B).

References

1. Hodes, G. Perovskite-based solar cells. *Science* **342,** 317–318 (2013).
2. Green, M. A., Ho-Baillie, A. & Snaith, H. J. The emergence of perovskite solar cells. *Nat. Photonics* **8,** 506–514 (2014).
3. Wu, J. *et al.* Electrolytes in dye-sensitized solar cells. *Chem. Rev.* **115,** 2136–2173 (2015).
4. Chen, W. *et al.* Efficient and stable large-area perovskite solar cells with inorganic charge extraction layers. *Science* **350,** 944–948 (2015).
5. Xiao, Z. *et al.* Efficient, high yield perovskite photovoltaic devices grown by interdiffusion of solution-processed precursor stacking layers. *Energy Environ. Sci.* **7,** 2619–2623 (2014).
6. Wehrenfennig, C. *et al.* High charge carrier mobilities and lifetimes in organolead trihalide perovskites. *Adv. Mater.* **26,** 1584–1589 (2014).
7. Stranks, S. D. *et al.* Electron-hole diffusion lengths exceeding 1 micrometer in an organometal trihalide perovskite absorber. *Science* **342,** 341–344 (2013).
8. Xing, G. *et al.* Long-range balanced electron- and hole-transport lengths in organic-inorganic $CH_3NH_3PbI_3$. *Science* **342,** 344–347 (2013).
9. D'Innocenzo, V. *et al.* Excitons versus free charges in organo-lead tri-halide perovskites. *Nat. commun.* **5,** 3586 (2014).
10. Bi, D. *et al.* Efficient luminescent solar cells based on tailored mixed-cation perovskites. *Sci. Adv*. **2(1),** e1501170 (2016).
11. Best Research-Cell Efficiencies. http://www.nrel.gov/pv/assets/images/efficiency_chart.jpg (2016-08-12).
12. Yang, W. *et al.* High-performance photovoltaic perovskite layers fabricated through intramolecular exchange. *Science* **348,** 1234–1238 (2015).
13. Kazim, S., Nazeeruddin, M., Gratzel, M. & Ahmad, S. Perovskite as light harvester: A game changer in photovoltaics. *Angew. Chem. Int. Ed.* **53,** 2812–2824 (2014).
14. Burschka, J. *et al.* Sequential deposition as a route to high-performance perovskite-sensitized solar cells. *Nature* **499,** 316–319 (2013).
15. Jeon, N. *et al.* Solvent engineering for high-performance inorganic-organic hybrid perovskite solar cells. *Nat. Mater.* **13,** 897–903 (2014).
16. Chen, Q. *et al.* Planar heterojunction perovskite solar cells via vapor-assisted solution process. *J. Am. Chem. Soc.* **136(2),** 622–625 (2014).
17. Liu, M., Johnston, M. & Snaith, H. Efficient planar heterojunction perovskite solar cells by vapour deposition. *Nature* **501,** 395–398 (2013).
18. Mei, A. *et al.* A hole-conductor-free, fully printable mesoscopic perovskite solar cell with high stability. *Science* **345,** 295–298 (2014).
19. Liang, P. W. *et al.* Additive enhanced crystallization of solution-processed perovskite for highly efficient planar-heterojunction solar cells. *Adv. Mater.* **26(22),** 3748–3754 (2014).
20. Yuan, D. X. *et al.* A solution-processed bathocuproine cathode interfacial layer for high-performance bromine-iodine perovskite solar cells. *Phys. Chem. Chem. Phys.* **17,** 26653–26658 (2015).
21. Yin, W. J., Yan, Y. & Wei, S. H. Anomalous alloy properties in mixed halide perovskites. *J. Phys. Chem. Lett*. **5,** 3625–3631 (2014).
22. Noh, J. H. *et al.* Chemical management for colorful, efficient, and stable inorganic-organic hybrid nanostructured solar cells. *Nano Lett.* **13,** 1764–1769 (2013).
23. Bi, C., Yuan, Y., Fang, Y. & Huang, J. Low-temperature fabrication of efficient wide-bandgap organolead trihalide perovskite solar cells. *Adv. Energy Mater*. **5,** 1401616 (2015).
24. Dong, Q. *et al.* Abnormal crystal growth in $CH_3NH_3PbI_{3-x}Cl_x$ using a multi-cycle solution coating process. *Energy Environ. Sci.* **8(8),** 2464–2470 (2015).
25. Dar, M. I. *et al.* Understanding the impact of bromide on the photovoltaic performance of $CH_3NH_3PbI_3$ solar cells. *Adv. Mater.* **27,** 7221–7228 (2015).
26. Yu, H. *et al.* Room-temperature mixed-solvent-vapour annealing for high performance perovskite solar cells. *J. Mater. Chem. A* **4(1),** 321–326 (2016).
27. Ge, Q. *et al.* Promoting crystalline grain growth and healing pinholes by water vapour modulated post-annealing for enhancing the efficiency of planar perovskite solar cells. *J. Mater. Chem. A* **4(35),** 13458–13467 (2016).
28. Zhou, Y. Y. *et al.* Room-temperature crystallization of hybrid-perovskite thin films via solvent-solvent extraction for high-performance solar cells. *J. Mater. Chem. A* **3(15),** 8178–8184 (2015).
29. Li, X. *et al.* A vacuum flash-assisted solution process for high-efficiency large-area perovskite solar cells. *Science* **353,** 58–62 (2016).
30. Zhou, Y. Y. *et al.* Manipulating crystallization of organolead mixed-halide thin films in antisolvent baths for wide-bandgap perovskite solar cells. *ACS Appl. Mater. Interfaces* **8,** 2232–2237 (2016).
31. Zheng, L. *et al.* Morphology control of the perovskite films for efficient solar cells. *Dalton Trans.*, **44(23),** 10582–10593 (2015).
32. Li, X. *et al.* Improved performance and stability of perovskite solar cells by crystal crosslinking with alkylphosphonic acid omega-ammonium chlorides. *Nature Chem*. **7,** 703–711 (2015).
33. Hou, Y. *et al.* Overcoming the interface losses in planar heterojunction perovskite-based solar cells. *Adv. Mater.* **28,** 5112–5120 (2016).
34. Murali, B. *et al.* Surface restructuring of hybrid perovskite crystals. *ACS Energy Lett*. **1,** 1119–1126 (2016).
35. Sutter-Fella, C. M. *et al.* High photoluminescence quantum yield in band gap tunable bromide containing mixed halide perovskites. *Nano Lett.* **16,** 800–806 (2016).
36. Huang, J. *et al.* Hydrobromic acid assisted crystallization of $MAPbI_{3-x}Cl_x$ for enhanced power conversion efficiency in perovskite solar cells. *RSC Adv*. **6,** 55720–55725 (2016).
37. Hagfeldt, A. *et al.* Dye-sensitized solar cells. *Chem. Rev.* **110,** 6596–6663 (2010).
38. Gratzel, M. Photoelectrochemical cells. *Nature* **414,** 338–344 (2001).
39. Rakstys, K. *et al.* Triazatruxene-based hole transporting materials for highly efficient perovskite solar cells. *J. Am. Chem. Soc.* **137(51),** 16172–16178 (2015).

40. Chen, H. *et al.* Solvent engineering boosts the efficiency of paintable carbon-based perovskite solar cells to beyond 14%. *Adv. Energy Mater*. **1502087** (2016).
41. Chen, S. *et al.* Exploring the limiting open-circuit voltage and the voltage loss mechanism in planar $CH_3NH_3PbBr_3$ perovskite solar cells. *Adv. Energy Mater*. **1600132** (2016).
42. Murali, B. *et al.* Temperature-induced lattice relaxation of perovskite crystal enhances optoelectronic properties and solar cell performance. *J. Phys. Chem. Lett.* **8,** 137–143 (2017).
43. Sun, Z., Zheng, H., Li, J. & Du, P. Extraordinarily efficient photocatalytic hydrogen evolution in water using semiconductor nanorods integrated with crystalline Ni_2P cocatalysts. *Energy Environ. Sci.* **8(9),** 2668–2676 (2015).
44. Gong, X. *et al.* Controllable perovskite crystallization by water additive for high-performance solar cells. *Adv. Funct. Mater.* **1503559** (2015).
45. Liu, D. *et al.* Compact layer free perovskite solar cells with 13.5% efficiency. *J. Am. Chem. Soc.* **136,** 17116–17122 (2014).
46. Son, D. *et al.* Effects of seed layer on growth of ZnO nanorod and performance of perovskite solar cell. *J. Phys. Chem. C* **119,** 10321–10328 (2015).
47. He, J. & Chen, T. Additive regulated crystallization and film formation of $CH_3NH_3PbI_{3-x}Br_x$ for highly efficient planar-heterojunction solar cells. *J. Mater. Chem. A* **3,** 18514–18520 (2015).
48. Chandiran, A. K. *et al.* Sub-nanometer conformal TiO_2 blocking layer for high efficiency solid-state perovskite absorber solar cells. *Adv. Mater.* **26,** 4309–4312 (2014).
49. Wu, J. H. *et al.* An all-solid-state dye-sensitized solar cell-based poly(N-alkyl-4-vinyl-pyridine iodide) electrolyte with efficiency of 5.64%. *J. Am. Chem. Soc.* **130,** 11568–11569 (2008).
50. Wu, J. H. *et al.* A novel thermosetting gel electrolyte for stable quasi-solid-state dye-sensitized solar cells. *Adv. Mater*. **19(22),** 4006–4011 (2007).
51. Tu, Y. *et al.* TiO_2 quantum dots as superb compact block layer for high-performance $CH_3NH_3PbI_3$ perovskite solar cells with efficiency of 16.97%. *Nanoscale* **7,** 20539–20546 (2015).

Acknowledgements

The authors acknowledge the financial joint support by the National Natural Science Foundation of China (Nos 91422301, 51472094, 61474047, U1205112), and the Cultivation Program for Postgraduate in Scientific Research Innovation Ability of Huaqiao University (No. 1400102002).

Author Contributions

J.W. conceived the project, J.W. and Y.T. designed the device and experiments, and Y.T. carried out most experiments. Y.T. wrote the first draft of the manuscript, and J.W. finished the submitted paper. All the authors Y.T., J.W., Z.L., X.H., J.D., J.J, P.G., J.L., M.H. and Y.H. discussed the results and approved publishing this paper.

Additional Information

Supplementary information accompanies this paper at http://www.nature.com/srep

Competing Interests: The authors declare no competing financial interests.

How to cite this article: Tu, Y. *et al.* Modulated $CH_3NH_3PbI_{3-x}Br_x$ film for efficient perovskite solar cells exceeding 18%. *Sci. Rep.* **7**, 44603; doi: 10.1038/srep44603 (2017).

Publisher's note: Springer Nature remains neutral with regard to jurisdictional claims in published maps and institutional affiliations.